APPLICATIONS OF
MODELLING AND SIMULATION
http://arqiipubl.com/ams eISSN 2600-8084 VOL 9, 2025, 303-314

Dynamic Control and Analysis of Dual Active Bridge Converters in Grid-Connected PV-BESS

Mehmet Can Sekanli*, Samet Yalçin and Okan Bingol

Department of Electrical - Electronics Engineering, Isparta University of Applied Sciences, Isparta, Türkiye

*Corresponding author: mehmetsekanli@isparta.edu.tr

Submitted 24 April 2025; Revised 24 June 2025; Accepted 30 June 2025; Available online 04 July 2025.

Abstract: Rising global energy demand, along with environmental concerns over greenhouse gas emissions, has made renewable energy systems increasingly important. Integrating photovoltaic (PV) arrays with battery energy storage systems (BESS) addresses the intermittent nature of solar energy effectively. This research focuses on simulating and analyzing a grid-connected PV-BESS configuration, incorporating a Dual Active Bridge (DAB) converter. The system was modelled using MATLAB/Simulink, with specifications including a 36-kW PV array, a 162-kWh battery, and a bidirectional power capability of 18 kW. The Perturb & Observe (P&O) Maximum Power Point Tracking (MPPT) algorithm optimized power extraction from the PV array, while the DAB converter employed Single Phase Shift (SPS) control for efficient, bidirectional energy management. Comprehensive testing across eight distinct scenarios showed reliable DC-link voltage control around 600 V and a notable reduction in inverter harmonic distortion (THD ≈ 2.5%). Overall, the simulation results confirm the robustness and practicality of the proposed design for improving grid-connected PV-BESS integration.

Keywords: Battery energy storage system (BESS); Bidirectional power flow; Dual active bridge (DAB) converter; Grid-connected PV systems.

1. INTRODUCTION

In recent years, factors such as population growth, economic development, urbanization, and industrialization have led to a significant increase in global energy consumption. This rise has also caused a considerable increase in greenhouse gas emissions. Given that greenhouse gas emissions directly contribute to climate change, many countries are turning to renewable energy sources and strongly pursuing green growth policies to mitigate this issue [1]. Among renewable energy sources, solar energy, derived from the abundant and clean energy of the sun, holds a significant place. However, the intermittent nature of solar energy, which can only generate power when sunlight is available, poses challenges for sustainable energy supply. At this point, energy storage systems come into play, enabling energy to be stored when the sun is active and this energy to be used when the sun is not active [2].

Bidirectional power converters play a vital role in storing and utilizing the energy obtained from solar power as needed [3, 4]. In energy storage systems, a variety of power converter topologies are widely utilized, including non-isolated types such as bidirectional buck-boost [5] and Ćuk [6], as well as isolated types such as Flyback [7], Push-Pull [8], Forward [9], Resonant [10], CLLC [11], and Dual Active Bridge (DAB) [12]. Among these topologies, the bidirectional buck-boost converter is commonly preferred due to its minimal component count, stable operation, and high efficiency at low power levels [5, 6]. However, its efficiency decreases at high power levels, and the voltage and current stress on the switching element increases. In contrast, power electronics topologies like the DAB converter, which use a higher number of switching elements, operate with high efficiency even at power transfers of 20 kW and above [7, 8]. Therefore, full-bridge bidirectional converter topologies like the DAB converter are preferred in high-power Grid-Connected PV-BESS. Studies in the literature indicate that energy storage systems are designed with limited capacities [13], the energy produced by hybrid renewable energy plants is predominantly used to supply AC loads [14] or simulations for grid-connected energy storage systems are conducted at low power levels [15]. Furthermore, while simulation studies addressing constant energy transfer in charging and discharging modes of PV systems exist, scenarios considering the continuity of PV production are lacking.

This paper presents a detailed analysis of the battery's state of charge (SoC) and voltage variations under different operational scenarios. The analyses consider the continuity of energy transferred to the grid during charging and discharging modes and evaluate the impact of high-power levels on system performance. The findings reveal that accurately modelling the effects of parameters such as SoC and voltage in Grid-Connected PV-BESS is crucial for effective energy management. In this context, the study lays a significant foundation for strategies that aim to improve the efficiency of energy storage systems.

The main contributions of the present study are as follows:

- A comprehensive and detailed mathematical model and simulation of a 36-kW grid-connected PV system integrated with a 162-kWh BESS using a DAB converter, specifically designed to ensure stable, continuous, and efficient bidirectional power management.
- Detailed analysis and modelling of power electronic components including PV arrays, boost converters employing the Perturb & Observe (P&O) Maximum Power Point Tracking (MPPT) algorithm, and the DAB converter operating with Single Phase Shift (SPS) control.
- Scenario-based performance evaluation through the simulation of eight realistic operational scenarios, focusing on constant 18 kW transfer to the grid under all operational conditions, evaluating battery behavior at varying SoC levels and irradiance conditions.
- In-depth interpretation of simulation outcomes, clearly demonstrating voltage stability, consistent dynamic battery behavior, and high system efficiency with THD = 2.5%.
- Establishment of foundational insights and guidelines for future studies aimed at enhancing system efficiency, stability, and scalability for larger-scale applications in renewable energy systems.

2. GRID CONNECTED PV-BESS

The Grid Connected PV-BESS's efficiently manages the energy generated by photovoltaic arrays, optimizing its usage throughout the day. During peak sunlight hours, the system directs the generated energy to both the grid and energy storage systems. When sunlight diminishes, it draws power from the storage system and the PV arrays to meet the grid's energy demands. This dynamic operation ensures a balance between energy production and consumption, reduces the strain on the grid, and makes stored energy readily available when needed. The structure of the Grid Connected PV-BESS is shown in Figure 1.

2.1 PV Array

A PV array is a system composed of interconnected solar panels, which consist of PV cells. Each PV cell is made from semiconductor materials designed to convert sunlight into electrical energy through the photovoltaic effect. Solar panels generate DC electricity, and the PV array serves as the core energy generation unit in solar energy systems. To increase the total power capacity of a PV array, solar panels can be configured in series or parallel connections. The energy production performance of a PV array is influenced by factors such as irradiance and temperature, as described in Equation (1).

$$I_{ph} = (I_{sc} + K * (T - 298)) * \left(\frac{G}{1000}\right) \quad (1)$$

where I_{ph} is the photocurrent (A), I_{sc} is the short-circuit current (A), K is the Boltzmann constant, T is the temperature in Kelvin (K), and G is the irradiance (W/m^2).

2.2 Boost Converter

In PV systems, boost converters are utilized to increase the voltage generated by the PV array and optimize energy efficiency. MPPT techniques are applied to regulate the duty cycle (D_{boost}) of the boost converter, which represents the ratio of the switch's ON time to the total switching period, thereby controlling the output voltage. The fundamental structure of the boost converter is illustrated in Figure 2.

The relationship between the duty cycle and the output voltage (V_{out}) of the boost converter is given by Equation (2).

$$V_{out} = \frac{V_{in}}{1 - D_{boost}} \quad (2)$$

where V_{in} is the input voltage (V).

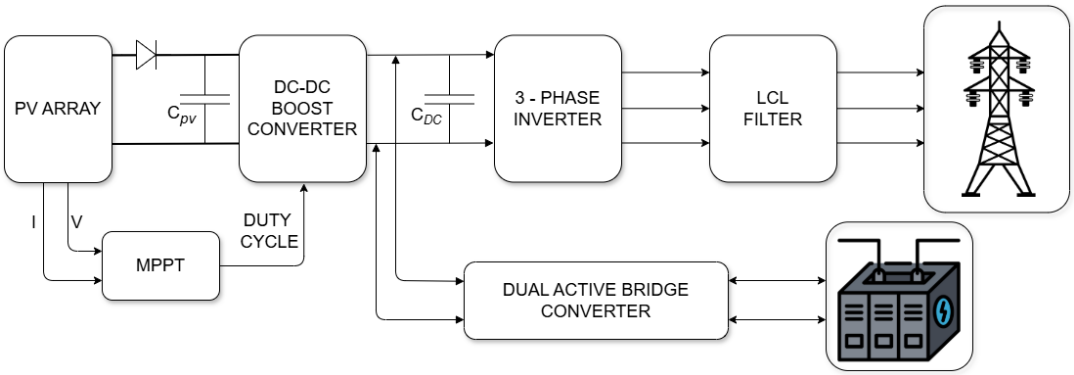

Figure 1. Grid connected PV-BESS.

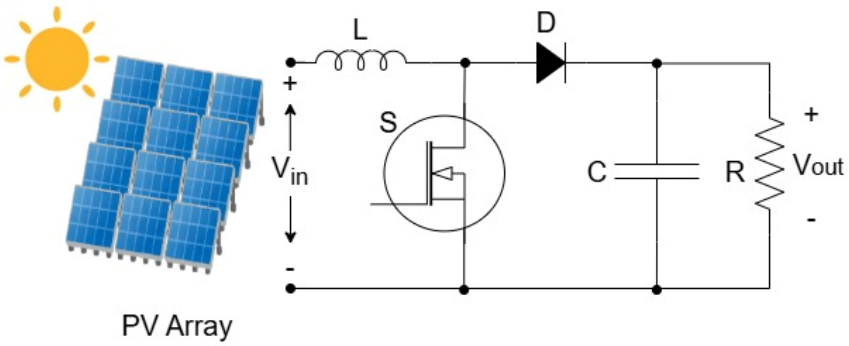

Figure 2. Boost converter.

Selecting appropriate inductor and capacitor values is crucial for the stable and efficient operation of the boost converter. The minimum inductance value (L_{min}) can be calculated by Equation (3):

$$L_{min} = \frac{D_{boost} * (1 - D_{boost})^2}{2 * f_{boost}} * \frac{{V_{out}}^2}{P} \tag{3}$$

where P is the output power (W), and f_{boost} is the switching frequency (Hz) of the boost converter. To ensure a safety margin, the actual inductance value is typically selected as at least 1.25 times greater than the minimum inductance calculated. Similarly, the required capacitance (C_{boost}) value for the boost converter can be determined by Equation (4):

$$C_{boost} = \frac{D_{boost}}{R * \left(\frac{\Delta V_o}{V_o}\right) * f_{boost}} \tag{4}$$

where ΔVo is the voltage ripple across the load resistance.

2.3 Perturb and Observe (P&O) Algorithm

P&O method is one of the most commonly used control algorithms in MPPT controllers [16]. Essentially, this method monitors the power change (dP) of the PV module and subsequently examines the corresponding voltage change (dV) to adjust the duty cycle (D) for optimal operation. Typically, the power-voltage (P-V) characteristic of the module is employed to observe the operating point and output power [17].

The decision criterion of this algorithm is based on evaluating the slope of the power-voltage curve (dP/dV), mathematically expressed as shown in Equation (5).

$$\frac{dP}{dV} = 0 \tag{5}$$

This relationship can further be defined as Equations (6) and (7).

$$dP = P(t) - P(t-1) \tag{6}$$

$$dV = V(t) - V(t-1) \tag{7}$$

where $P(t)$ is the power measured at the current step, $P(t-1)$ is the power measured at the previous step, $V(t)$ is the voltage measured at the current step and $V(t-1)$ is the voltage measured at the previous step. A positive slope $(dP/dV>0)$ suggests that the operating point is located to the left of the MPP, while a negative slope $(dP/dV<0)$ indicates that the point is on the right side of the MPP. The tracking process iterates multiple times until the slope reaches zero $(dP/dV=0)$, signifying that the MPP has been successfully tracked. The number of perturbations per second is defined as the perturbation frequency, which can also be interpreted as the operating frequency of the MPPT algorithm [23]. Figure 3 illustrates the flowchart of the P&O method.

2.4 Dual Active Bridge Converter

DAB converters are critical components in Grid-Connected PV-BESS systems due to their ability to achieve high-power bidirectional energy transfer, high efficiency, compact size, and natural zero-voltage switching (ZVS), which occurs when the input and output voltage ratio aligns with the transformer turns ratio [12, 15, 18, 19].

Compared to traditional converters, the Dual Active Bridge (DAB) converter stands out in the literature due to features such as galvanic isolation, a wide soft-switching range, modular structure, high power density [18, 20], reduced switching losses, and a successful balance between electromagnetic interference (EMI) and efficiency [21, 22, 23]. A DAB converter consists of two bridges (primary and secondary) connected via a high-frequency transformer, as shown in Figure 4.

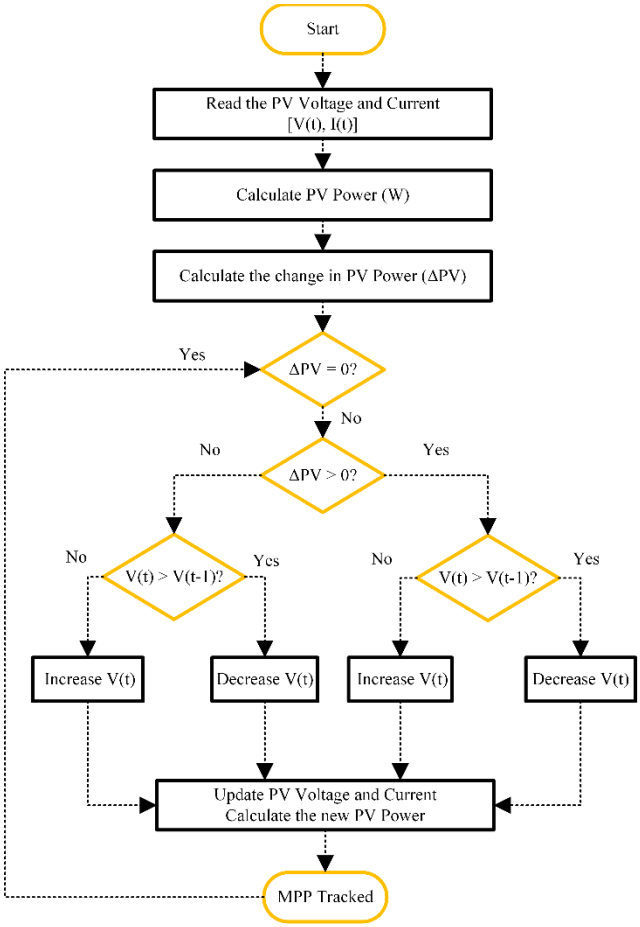

Figure 3. Flowchart of the P&O method.

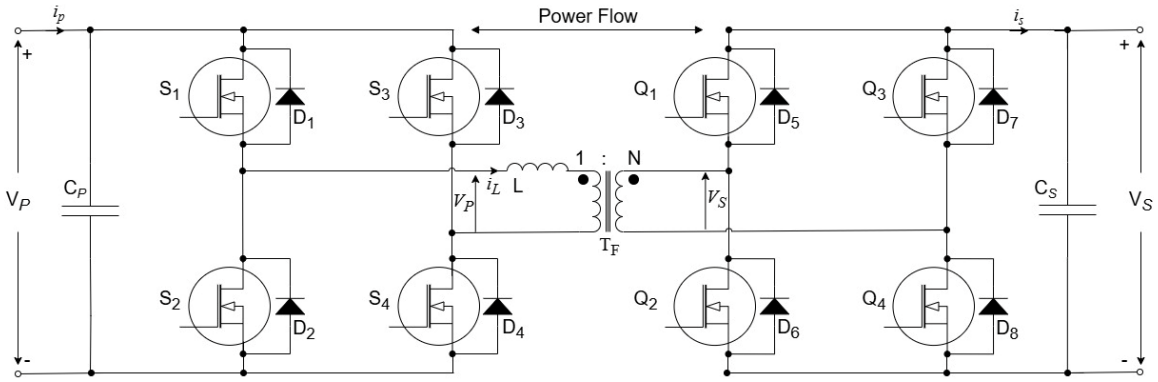

Figure 4. Dual active bridge converter.

The DAB converter fundamentally includes four distinct phase-shift modulation methods: Triple phase shift (TPS), double phase shift (DPS), extended phase shift (EPS), and SPS [24]. Among these, the most comprehensive method is TPS. The TPS technique features six operating modes based on the phase shifts between switching elements, making it a detailed and complex switching strategy. The DPS method, which offers symmetric phase shifting, operates in either the sixth or third mode of TPS. The EPS method typically operates in the sixth, first, or second mode. In contrast, SPS is a phase-shift method that operates solely in the sixth mode [25]. As can be inferred, SPS is the simplest and most widely used method in the industry, capable of operating within the DAB converter's natural soft-switching range. Unlike other phase-shift techniques—which involve controlling multiple (at least three) independent phase shifts - the SPS method simplifies control by adjusting just a single-phase shift between the primary and secondary bridges [26, 27, 28]. Therefore, in this study the SPS method was utilized.

The output power of a DAB converter using the SPS method is given by Equation (8).

$$P_o = \frac{V_p * V_s * N_{ps}}{2 * f_{sw} * L_{lk}} * D_{DAB} * (1 - D_{DAB}) \tag{8}$$

where P_o is the output power (W), V_p is the DC voltage at the side of the primary full bridge (V), V_s is the DC voltage at the side of the second full bridge (V), N_{ps} is the primary-to-secondary turns ratio of the transformer, f_{sw} is the switching frequency (Hz),

L_{lk} is the leakage inductance (H), and D_{DAB} is the phase shift ratio, ranging from 0 to 1. The output power is maximized when $D_{DAB} = 0.5$.

There are three conditions for achieving soft switching operation in the DAB converter. These criteria ensure efficient converter performance at both small and large phase shift angles and are dependent upon the voltage conversion ratio (*d*). The first condition defines the relationship between the transformer's turns ratio and the voltage conversion ratio, as given in Equation (9).

$$d = \frac{V_p}{N_{ps} * V_s} \tag{9}$$

For soft-switching on the primary full-bridge side, the phase shift ratio D_{DAB} needs to satisfy the condition expressed in Equation (10):

$$D_{DAB} > \frac{1}{2}(1 - d) \tag{10}$$

Similarly, for soft-switching on the secondary full-bridge side, the phase shift ratio D_{DAB} should fulfill the condition expressed in Equation (11):

$$D_{DAB} > \frac{1}{2}(1 - \frac{1}{d}) \tag{11}$$

Satisfying these equations ensures stable and highly efficient operation of the DAB converter, effectively minimizing power conversion losses [19, 29].

2.5 Battery Energy Storage System

BESS was designed to deliver a continuous 18 kW power output to the grid. To determine the required capacity of the BESS, the total energy demand during non-sunlight hours was calculated by multiplying the number of hours without sunlight by the desired power output, as expressed in Equation (12):

$$E_{BESS} = P_{BESS} \times t \tag{12}$$

where E_{BESS} is the battery storage capacity (kWh), P_{BESS} is the continuous power output to the grid (kW), and *t* is the duration without solar energy (*h*). Considering an average of 9 hours of full sunlight per day, the required energy storage capacity was derived accordingly. Since the DC bus voltage was set to 600 V to ensure compatibility with the DAB converter operating in ZVS mode, the BESS voltage was also set to 600 V. Based on this voltage, the required current capacity of the BESS(Q_{BESS}) was determined by dividing the calculated energy capacity by the selected voltage, as shown in Equation (13):

$$Q_{BESS} = \frac{E_{BESS}}{V_{BESS}} \tag{13}$$

where Q_{BESS} is the battery current capacity (Ah) and V_{BESS} is the nominal voltage of the battery system (V).

2.6 Voltage Source Inverter

In this study, a three-phase Voltage Source Inverter (VSI) controlled with Sinusoidal Pulse Width Modulation (SPWM) was implemented to convert the generated and stored DC energy into AC power suitable for grid connection. The three-phase design ensures balanced and efficient energy transfer to the grid, meeting standard grid compatibility requirements. MOSFET switches were selected for their rapid switching capabilities and efficiency. SPWM generates inverter switching signals by continuously comparing a sinusoidal reference waveform with a high-frequency triangular waveform. Switches activate whenever the sinusoidal reference surpasses the carrier signal, resulting in a smooth, near-sinusoidal output waveform. This method effectively reduces harmonic distortion, thus ensuring high-quality power output and compliance with grid connection standards.

2.7 LCL Filter

Inverter outputs commonly contain unwanted harmonics due to the high-frequency switching actions. An LCL filter is implemented at the inverter output to effectively suppress these harmonics, improving the quality of AC power delivered to the grid. Compared to simpler L or LC filters, the LCL configuration—consisting of two inductors and one capacitor arranged in a specific sequence—offers superior harmonic attenuation, better damping characteristics, and lower voltage drops. Additionally, the compactness and efficiency of LCL filters, even at reduced switching frequencies, make them highly suitable for modern high-power inverter applications, significantly enhancing overall system performance and grid compliance.

3. MODELLING AND SIMULATION METHODOLOGY

In this study, the proposed Grid Connected PV-BESS system is designed using Matlab/Simulink. The Matlab/Simulink implementation of the Grid Connected PV-BESS depicted in Figure 1 is presented in Figure 5.

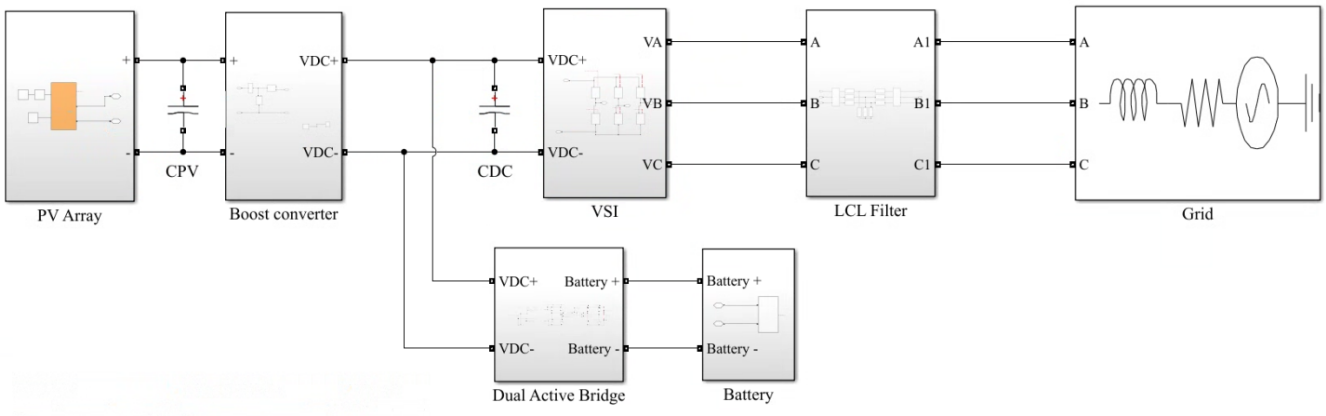

Figure 5. Simulink model of the grid-connected PV-BESS system topology.

A 36-kW PV array configuration is implemented, and maximum efficiency is achieved from the PV array through a boost converter and P&O MPPT method. The parameters of the PV array at the initial stage of the design, illustrated in Figure 1, were determined using a selected PV module according to Equation (1). The total power output of the PV array was set to 36 kW and was achieved by configuring the modules through a combination of series and parallel connections. This output was calculated based on the module's rated power, the number of modules connected in series per string, and the number of parallel strings, as expressed in Equation (14).

$$P_{array} = N_{series} \times N_{parallel} \times P_{module} \tag{14}$$

where P_{module} is the rated power of a single PV module, N_{series} is the number of modules connected in series and $N_{parallel}$ is the number of parallel strings. These parameters are summarized in Table 1. The Boost converter circuit modeled in Simulink was designed based on Equations (2), (3) and (4) and the calculated component values are presented in Table 2.

The Matlab/Simulink model of the DAB converter circuit is represented as a subsystem within Figure 5. In the DAB converter simulation, both the input and nominal output voltage of the DAB converter were set to 600 V, and N was selected as 1 to ensure natural ZVS operation. To achieve a maximum power transfer of 18 kW at a switching frequency of 250 kHz, L_{lk} was chosen as 6 µH. For battery voltages ranging from 376 V to 686 V, D_{DAB} was calculated to be 0.4 and 0.155, respectively. The DAB converter specifications are summarized in Table 3. The designed BESS was implemented using LiFePO4 cells, configured as 188S45P to achieve the necessary voltage and current requirements. The BESS specifications are summarized in Table 4. LCL filter component values are detailed in Table 5.

Table 1. PV array parameters.

Parameters	Value
PV module power (W)	213.15
Paralel strings	17
Series connected modules per string	10
PV array power (kW)	36

Table 2. Boost converter parameters.

Parameters	Value
Switching frequency (kHz)	100
Inductor (µH)	6
Capacitance (µF)	34
Output Voltage (V)	600
Maximum Output Current (A)	60

Table 3. DAB converter parameters.

Parameters	Value
Input Voltage (V)	600
N	1
Switching Frequency (kHz)	250
Leakage Inductance (µH)	6

Table 4. BESS parameters.

Parameters	Value
BESS Capacity (kWh)	162
Cell Type	LiFePO4 (3.2 V)
BESS Max Power (kW)	18
Nominal Voltage (V)	600
Current Capacity (Ah)	270
Maximum Current (A)	810

Table 5. LCL filter parameters.

Parameters	Value
L_{in} (mH)	0.438
L_{out} (mH)	0.438
C_f (mF)	0.012

4. OPERATING CONDITIONS OF PROPOSED MODEL FOR GRID CONNECTED PV-BESS

Simulation scenarios are applied in grid-connected PV-BESS systems in literature. Sharma and Gupta [30] created a scenario with a fixed radiation level. However, this paper presents different irradiation levels. In this paper, to evaluate the dynamic performance under varying environmental and battery conditions, eight operating points were defined by combinations of PV generation, SoC, and power flow direction. The key parameters for each scenario are summarized in Table 6.

Table 6. Power flow parameters for different operating scenarios.

Scenario	PV Power (kW)	Power to Grid (kW)	Power to Battery (kW)	Battery SoC (%)	Irradiation (W/m²)
9C20	27	18	9	20	750
9C80	27	18	9	80	750
9D20	9	18	-9	20	250
9D80	9	18	-9	80	250
18C20	36	18	18	20	1000
18C80	36	18	18	80	1000
18D20	0	18	-18	20	0
18D80	0	18	-18	80	0

Under moderate irradiance (750 W/m²), scenarios 9C20 and 9C80 represent daytime charging: a 27-kW PV array delivers 18 kW to the grid while charging the battery at 9 kW, starting from 20% and 80% SoC, respectively. In the afternoon under low irradiance (250 W/m²), scenarios 9D20 and 9D80 simulate discharging: a 9-kW PV contribution is supplemented by a 9-kW battery discharge to sustain an 18-kW grid feed, highlighting the influence of initial SoC on discharge dynamics. High-irradiance charging is examined in scenarios 18C20 and 18C80, where a 36-kW PV output splits evenly between the grid and battery (18 kW each) at 20% and 80% SoC. Finally, nighttime discharging is modeled in scenarios 18D20 and 18D80, with zero PV production requiring the battery to supply the full 18-kW grid demand, demonstrating the impact of SoC on high-power discharge behavior.

5. RESULTS AND DISCUSSION

In this study, the proposed Grid-Connected PV-BESS system was tested under eight different scenarios. Figure 6 illustrates the power output of the PV system under varying irradiation levels. The graph compares the PV module's power output over time at irradiation levels of 0 W/m², 250 W/m², 750 W/m², and 1000 W/m². For each scenario, the irradiation level is maintained constant throughout the observation period. As observed, the power output increases linearly with higher irradiation levels. Specifically, at 1000 W/m², the PV system produces approximately 36 kW of power, whereas at 0 W/m², no power is generated. These results clearly demonstrate the critical impact of constant irradiation levels on the performance of the PV module.

Figure 7 presents the DC link voltage profiles under various operational scenarios (a-h). In the four charging scenarios (9C20, 9C80, 18C20, 18C80) the PV-array/boost-converter pair is the dominant energy source. Because the boost converter regulates current under the guidance of the MPPT loop, the PV side behaves like a low-impedance voltage source that quickly re-fills the DC-link capacitor after any disturbance. As a result, the initial overshoot or undershoot is modest (≈ ±4 V from the 600 V set-point) and the link voltage settles into the 596–602 V band within roughly 0.12 s. The 18 kW cases even damp slightly faster than the 9 kW cases, since the higher PV power recharges the capacitor more vigorously, tightening regulation despite the larger absolute current flow to the battery.

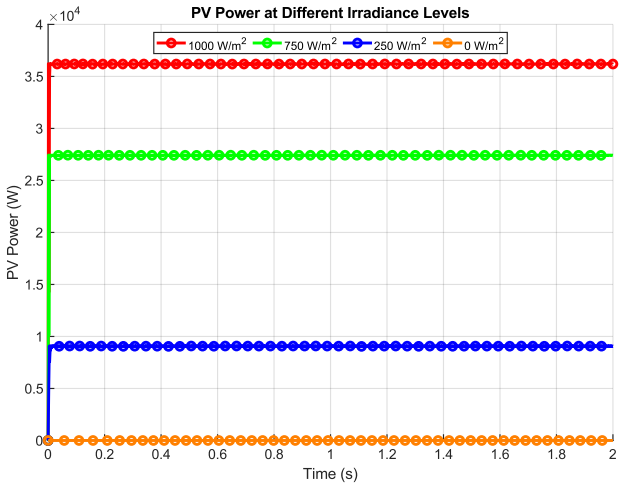

Figure 6. PV power at different irradiance levels.

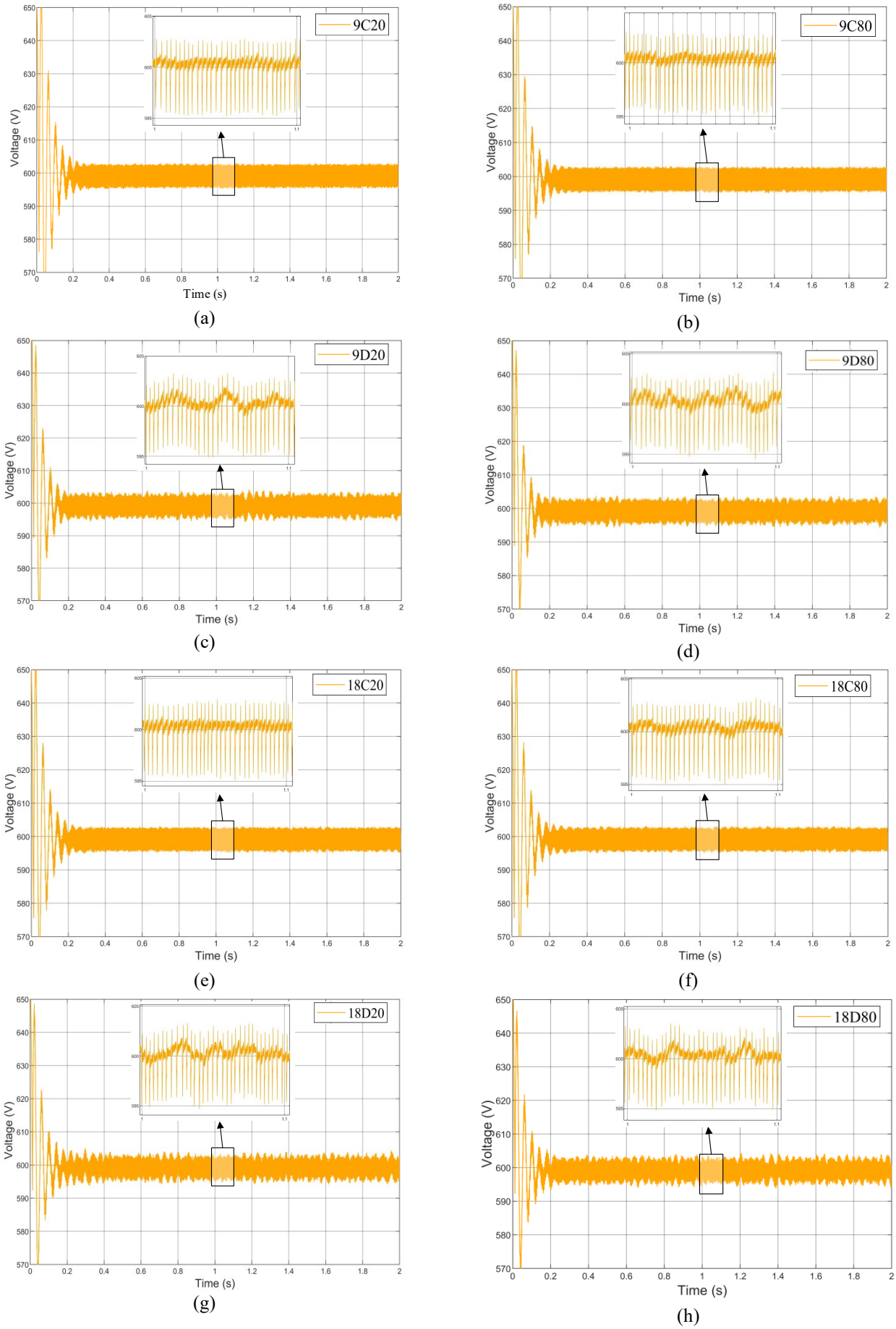

Figure 7. DC link voltage profiles for different operational scenarios: (a) 9C20, (b) 9C80, (c) 9D20, (d) 9D80, (e) 18C20, (f) 18C80, (g) 18D20, (h) 18D80.

By contrast, in the four discharging scenarios (9D20, 9D80, 18D20, 18D80) the battery, through the DAB converter, becomes the sole or principal source feeding both the inverter and the DC-link. Here the SPS-controlled DAB regulates power rather than voltage: any transient phase-shift error momentarily mismatches battery power and load demand, forcing the DC-link capacitor to absorb that difference. Coupled with the battery's internal resistance and finite electro-chemical response, this yields deeper oscillations (≈ ±6 V) and a slightly longer settling time of ~0.15 s. Even so, all discharging cases converge to the same 600 ± 2 V steady state before 0.2 s, demonstrating that the combined DAB, inverter, and PI control loops provide sufficient damping and robustness when the battery is the dominant energy source.

Examining the battery voltage values presented in Figure 8, significant differences can be observed between the charging modes (charge modes - 9C20, 9C80, 18C20, 18C80) and the discharging modes (discharge modes - 9D20, 9D80, 18D20, 18D80). Particularly, the 18 kW charging modes (18C20, 18C80) show a faster stabilization (steady state) compared to other modes, with the battery voltage reaching a higher level. This indicates that as the amount of power transferred to the battery increases, the battery voltage rises more quickly, allowing the system to reach steady state in a shorter time. In the charging modes, the battery voltage increases in direct proportion to power transfer. In contrast, in the discharging modes (9D20, 9D80, 18D20, 18D80), a decrease in battery voltage is observed as power is transferred from the battery to the grid. This reduction in voltage results from the power transfer from the battery to the grid. Additionally, a difference in starting voltage is evident between the 20% and 80% SoC levels. In the 20% SoC scenarios, the initial voltage of the battery is lower, while in the 80% SoC scenarios, a higher initial voltage is observed. These results clearly demonstrate how the battery voltage changes with the direction and magnitude of power flow in the system. Specifically, at higher power levels like 18 kW, the system's fast response highlights the fast dynamic performance of the proposed Grid Connected PV-BESS.

Figure 9 shows battery states at two initial SoC levels: (a) 20% and (b) 80%. In the charging modes (9C20, 18C20, 9C80, 18C80), the SoC level increases over time in a linear manner, while in the discharging modes (9D20, 18D20, 9D80, 18D80), the SoC level decreases linearly. The 18-kW charging and discharging modes show a faster change in the SoC level, indicating that the battery undergoes quicker charging and discharging at higher power levels. This linear change reflects a consistent energy flow, which is particularly noticeable in the higher-power scenarios (18 kW), where the battery's response to charging and discharging is faster and more direct.

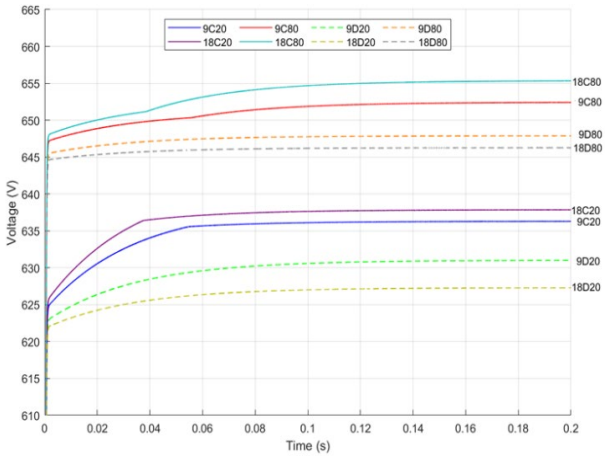

Figure 8. Battery voltages.

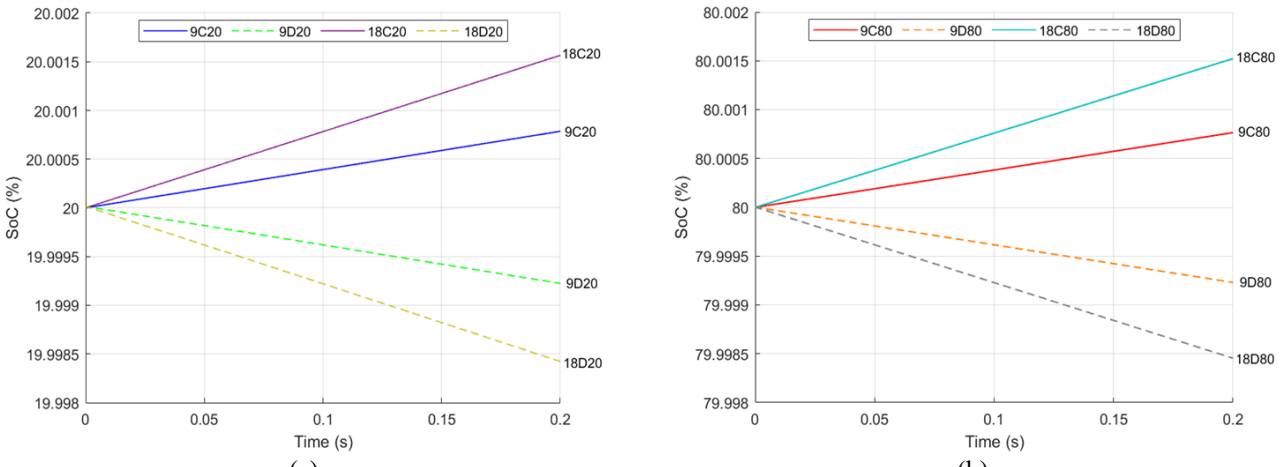

(a) (b)

Figure 9. Battery states at initial SoC levels of (a) 20% and (b) 80%.

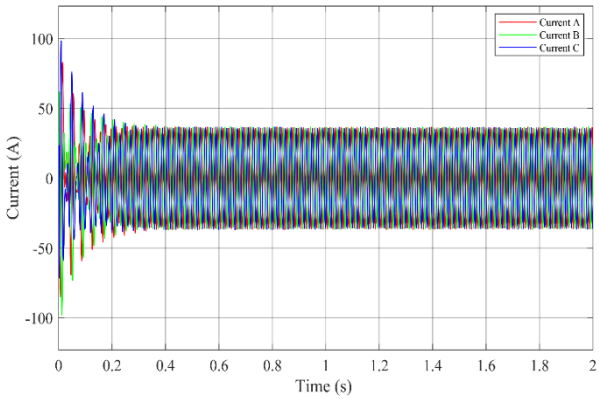

Figure 10. Three-phase current waveforms demonstrating transient and steady-state behaviors under constant 18 kW power transfer.

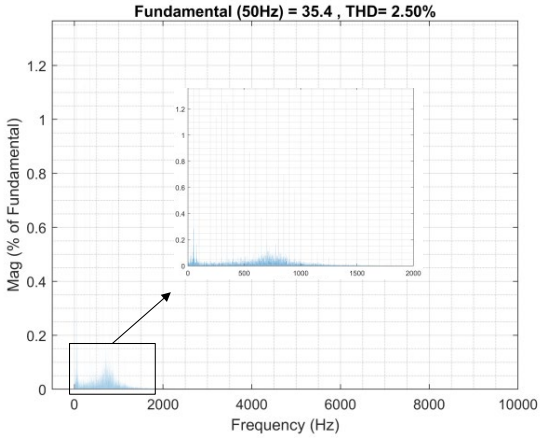

Figure 11. Frequency spectrum analysis indicating harmonic distribution and THD of the system output current.

The graph presented in Figure 10 illustrates the three-phase system currents (phases A, B, and C) as a function of time. Initially, the currents exhibit damped oscillations, which gradually diminish until the system reaches a stable operating condition at approximately 0.2 seconds. After this transient period, the phase currents stabilize and maintain a consistent sinusoidal waveform, indicating that the control strategy effectively ensures steady-state operation. Moreover, since the system consistently transfers a continuous power of 18 kW, this steady-state behavior confirms the robustness and stability of the implemented power control method. The observed transient behavior during system start-up—characterized by diminishing oscillations—suggests effective damping and rapid settling characteristics inherent in the designed control scheme. Consequently, the system demonstrates favorable dynamic performance and reliability under continuous power transfer conditions, validating its suitability for practical grid-connected renewable energy applications.

The frequency spectrum presented in Figure 11 shows the harmonic analysis of the inverter output current waveform, with a fundamental frequency of 50 Hz and a fundamental magnitude of 35.4 units. The system's calculated THD is found to be 2.50%, indicating a significant reduction in harmonic content after filtering. The inset figure provides a zoomed-in view of the lower-frequency region (up to approximately 2000 Hz), clearly illustrating that the amplitude of harmonic components decreases substantially as frequency increases. This demonstrates the effectiveness of the implemented LCL filter in attenuating harmonics, especially at frequencies higher than the fundamental. Given the achieved low THD value (<5%), the resulting current waveform aligns well with standard grid codes, validating the efficiency and effectiveness of the designed filtering strategy and control approach used in this Grid-Connected PV-BESS application.

In scenarios 9C20 and 9C80, the PV system generates 27 kW of power under 750 W/m² irradiance. Of this power, a constant value of 18 kW is directly transferred to the grid, while the surplus 9 kW charges the battery. Despite both scenarios having the same power flow values, the initial SoC levels differ (20% vs. 80%), affecting the battery's voltage and charge dynamics. For scenarios 9D20 and 9D80, the PV array generates only 9 kW under 250 W/m² irradiance. Since the system aims to continuously supply 18 kW to the grid, an additional 9 kW is drawn from the battery, indicating discharging operation. Again, battery response differs according to the initial SoC conditions, which significantly impacts battery voltage and discharge behavior. In scenarios 18C20 and 18C80, the PV system operates under 1000 W/m² irradiance, generating 36 kW power. In these conditions, the PV system delivers a total power of 36 kW, allocating 18 kW directly to the grid while simultaneously charging the battery with the remaining 18 kW. Compared to scenarios with lower power levels, these high-power scenarios demonstrate faster battery voltage stabilization and quicker battery charging. Lastly, scenarios 18D20 and 18D80 depict nighttime conditions with no PV generation, requiring the battery to supply the entire 18 kW power to the grid. These scenarios demonstrate the battery's capability for sustained high-power discharge. The thorough analysis of all these scenarios highlights the efficiency and reliability of the proposed energy management approach, verifying that the system consistently provides a stable 18 kW output to the grid across a variety of PV and battery operating conditions.

6. CONCLUSION

This paper presents a grid-connected PV-BESS utilizing a DAB converter that was controlled and thoroughly analyzed under various operational conditions, including different power flow scenarios and battery SoC levels. Recent studies have shown that the energy production system works well with the grid [30, 31]. However, in this study, we have demonstrated that a battery-backed system also has the desired harmonic and SoC parameters.

Key findings and implications:

- The grid-connected PV-BESS system with the DAB converter effectively handled dynamic energy flows under diverse conditions, consistently regulating the DC-link voltage near 600 V, and ensuring fast stabilization of battery voltage and SoC.
- The system maintained robust performance with minimal voltage oscillations, confirming systems reliability and superior response at high power transfer scenarios.

- Harmonic distortion in inverter output was significantly reduced, achieving a THD of 2.5% through the use of a three-phase inverter with SPWM control and a carefully designed LCL filter. This ensures compliance with stringent grid-quality standards.

Limitations of the study:

- The study relies exclusively on simulation results, which present inherent limitations. The actual performance of the proposed system and the precision of the control strategies could vary in practical, real-world implementations. Consequently, the reliability of the proposed system and control strategies must be verified experimentally before industrial implementation.

Practical implications:

- The demonstrated capability of the PV-BESS system to reliably manage energy transfers under varying conditions emphasizes its significant potential for real-world renewable energy applications. This reliability is particularly beneficial for scenarios requiring continuous high-power delivery to the grid.
- The insights and analysis provided by this study offer valuable guidelines for the practical design and deployment of efficient renewable energy management systems. These contributions reinforce the practicality, scalability, and robustness necessary for widespread adoption in real-world energy systems.

Recommendations for future research:

- Conducting experimental validations to confirm and compare simulation results with actual performance.
- Exploring advanced control techniques to further improve the efficiency of DAB converters.
- Developing strategies for optimizing scalability and implementation in large-scale PV-BESS applications.

ACKNOWLEDGEMENT AND FUNDING

The authors receive no financial support for the research, authorship, and publication of this article.

DECLARATION OF CONFLICTING INTERESTS

The authors declare no potential conflicts of interest with respect to the research and publication of this article.

REFERENCES

[1] A. Allouhi, S. Rehman, M. S. Buker and Z. Said, Recent technical approaches for improving energy efficiency and sustainability of photovoltaic (PV) and photovoltaic–thermal (PV-T) systems: A comprehensive review, *Sustainable Energy Technologies and Assessments*, 56, 2023, 103026.

[2] Q. Peng, A. Sangwongwanich, Y. Yang and F. Blaabjerg, Grid-friendly power control for smart photovoltaic systems, *Solar Energy*, 210, 2020, 115-127.

[3] X. Wu and T. Kerekes, Flexible active power control for photovoltaic–energy storage system (PV-ESS) systems: A review, *Energies*, 14, 21, 2021, 7388.

[4] T. Sutikno, R. A. Aprilianto and H. S. Purnama, Application of non-isolated bidirectional DC–DC converters for renewable and sustainable energy systems: A review, *Clean Energy*, 7, 2023, 293-311.

[5] Y. Zhang, C. Sun, S. Wang, Y. Shen and Z. Chen, Bidirectional buck–boost converter-based active power decoupling method for single-phase photovoltaic grid-connected inverters, *Journal of Power Electronics*, 25, 2, 2025 193-204.

[6] V. D. V., V. K. Pandraka, J. Gurram and S. Chapala, Design and implementation of average current mode control of solar PV fed bidirectional Čuk converter for battery energy storage systems, *Proceedings of the IEEE International Conference on Smart Power Control and Renewable Energy*, Rourkela, India, 2024, 1-6.

[7] G. H. Min and J. I. Ha, Inner supply data transmission in quasi-resonant flyback converters for lithium-ion battery applications using multiplexing mode, *IEEE Transactions on Power Electronics*, 34, 1, 2018, 64-73.

[8] M. B. El Kattel, R. Mayer, M. D. Possamai and S. Vidal Garcia Oliveira, Bidirectional isolated three-phase DC–DC converter using coupled inductor for direct-current microgrid applications, *International Journal of Circuit Theory and Applications*, 48, 6, 2020, 832-859.

[9] Y. E. Wu and I. C. Chen, Novel integrated three-port bidirectional DC–DC converter for energy storage systems, *IEEE Access*, 7, 2019, 104601-104612.

[10] A. Lichev, Y. Madankov, V. Mihov and D. Spirov, Bidirectional resonant power converter for hybrid energy systems, *Engineering Proceedings*, 70, 1, 2024, 3.

[11] R. Emamalipour and J. Lam, A multi-mode full-bridge/modified-stacked-switches structured CLLC resonant converter for energy storage applications, *IEEE Transactions on Power Electronics*, 39, 5, 2024, 5967-5981.

[12] A. Agrawal, Circulating power flow restricted operation of the isolated bidirectional dual-active-bridge DC–DC converter for battery charging applications, *Journal of Energy Storage*, 86, 2024, 111123.

[13] D. B. Aeggegn, G. N. Nyakoe and C. Wekesa, ANFIS-controlled boost and bidirectional buck-boost DC–DC converters for solar photovoltaic, fuel cell, and battery energy storage systems–based microgrid applications, *International Transactions on Electrical Energy Systems*, 2024, 6484369.

[14] M. E. Şahin and F. Blaabjerg, Photovoltaic-powered hybrid energy storage system control using bidirectional and boost converters, *Electric Power Components and Systems*, 49, 15, 2022, 1260-1277.

[15] Z. Zhang, J. Sun, P. Wang, Z. Cai, J. Kong, X. Bai and D. Ma, An improved direct-current bias elimination strategy with extended phase shift control for dual-active-bridge DC–DC converters, *Proceedings of the Chinese Automation Congress*, Hangzhou, China, 2019, 4274-4279.

[16] J. A. Jiang, Y. L. Su, K. C. Kuo, C. H. Wang, M. S. Liao, J. C. Wang et al., On a hybrid maximum power point tracking control scheme to improve energy harvesting performance of traditional two-stage inverters used in photovoltaic systems, *Renewable and Sustainable Energy Reviews*, 69, 2017, 1113-1128.
[17] M. A. Elgendy, B. Zahawi and D. J. Atkinson, Assessment of perturb and observe maximum power point tracking algorithm implementation techniques for photovoltaic pumping applications, *IEEE Transactions on Sustainable Energy*, 3, 1, 2011, 21-33.
[18] Texas Instruments, *Design Guide: TIDA-010054 Bidirectional Dual Active Bridge Reference Design for Level 3 Electric Vehicle Charging Stations*, 2022.
[19] J. Huang, Y. Wang, Z. Li and W. Lei, Unified triple-phase-shift control to minimize current stress and achieve full soft-switching of isolated bidirectional DC–DC converters, *IEEE Transactions on Industrial Electronics*, 63, 7, 2016, 4169-4179.
[20] Y. A. Harrye, K. H. Ahmed, G. P. Adam and A. A. Aboushady, Comprehensive steady-state analysis of bidirectional dual active bridge DC–DC converters using triple phase shift control, *Proceedings of the IEEE International Symposium on Industrial Electronics*, Istanbul, Turkiye, 2014, 437-442.
[21] K. D. Hoang and J. Wang, Design optimization of high-frequency transformer for dual active bridge DC–DC converters, *Proceedings of the XXth International Conference on Electrical Machines*, Marseille, France, 2012, 2311-2317.
[22] S. A. Gorji, H. G. Sahebi, M. Ektesabi and A. B. Rad, Topologies and control schemes of bidirectional DC–DC power converters: An overview, *IEEE Access*, 7, 2019, 117997-118019.
[23] X. Fei, Z. Feng, N. PuQi and W. Xuhui, Analyzing zero-voltage-switching soft-switching using single phase shift control strategy of dual-active-bridge isolated DC–DC converters, *Proceedings of the International Conference on Electrical Machines and Systems*, Jeju, Korea (South), 2018, 2378-2381.
[24] B. Zhao, Q. Song, W. Liu and Y. Sun, Overview of dual-active-bridge isolated bidirectional DC–DC converters for high-frequency-link power-conversion systems, *IEEE Transactions on Power Electronics*, 29, 8, 2013, 4091-4106.
[25] S. Yalçın, *Analysis and Suppression of Electromagnetic Interference Caused by Silicon Carbide–Based Dual Active Bridge Converters*, Ph.D. dissertation, Isparta University of Applied Sciences, Isparta, Turkiye, 2023.
[26] X. Chen, G. Xu, H. Han, D. Liu, Y. Sun and M. Su, Light-load efficiency enhancement of high-frequency dual-active-bridge converters under single phase shift control, *IEEE Transactions on Industrial Electronics*, 68, 12, 2020, 12941-12946.
[27] F. Corti, V. Bertolini, A. Reatti, E. Cardelli and M. Giallongo, Comparison of control strategies for dual active bridge converters, *Proceedings of the IEEE Mediterranean Electrotechnical Conference*, Palermo, Italy, 2022, 902-907.
[28] E. K. Effah, E. K. Anto, P. Y. Okyere and F. B. Effah, Model reference adaptive control of single phase shift–based dual active bridge converters with constant power loading, *Power Electronics and Drives*, 9, 2024.
[29] S. Zengin, *Single-Stage Dual Active Bridge AC–DC Converter Using Silicon Carbide Power Switches*, Ph.D. dissertation, Ege University Graduate School of Natural and Applied Sciences, Izmir, Turkiye 2019.
[30] G. Sharma and R. Gupta, Solar photovoltaic based grid-scale battery energy storage system with interleaved boost converter and dual active bridge, *Proceedings of the International Conference on Computer Applications in Electrical Engineering – Recent Advances*, Roorkee, India, 2023, 1-6.
[31] M. K. Kar, S. Kanungo, S. Dash and R. R. Parida, Grid-connected solar panel with battery energy storage system, *International Journal of Applied Sciences*, 13, 1, 2024, 223-233.